

APPLICATION OF SPACE-TIME MAPPING ANALYSIS METHOD TO UNSTEADY NONLINEAR GUST-AIRFOIL INTERACTION PROBLEM

Vladimir V. Golubev* and Axel Rohde†

Embry-Riddle Aeronautical University
Daytona Beach, FL 32114

ABSTRACT

This paper is concerned with the application of a new Space-Time Mapping Analysis (STMA) method to a nonlinear, inviscid computation of unsteady airfoil response to an impinging, high-intensity, vortical gust. The method solves the unsteady problem as a steady-state one by treating the time coordinate identically to the space directions. A high-order discretization scheme is provided to achieve time-accurate predictions of both unsteady aerodynamic and aeroacoustic responses. The obtained results show localized zones in the computational plane where nonlinear response effects become important.

INTRODUCTION

In this work, a new numerical approach presented in Ref. [1] is applied to the nonlinear analysis of the unsteady gust-airfoil interaction problem. The new Space-Time Mapping Analysis (STMA) method has been developed to effectively treat any two- or three-dimensional unsteady problem as a steady-state one in a three- or four-dimensional space. This approach essentially paves the way for extending high-accuracy discretization schemes developed in Computational Aeroacoustics (CAA) for spatial derivatives to the time derivative, thus achieving highly time-accurate computations with absolute stability. It appears to provide additional flexibility of clustering the space-time grid in regions of rapid solution changes, and is well-suited for distributed-memory parallel processing.

The traditional prediction methods employed in the field of Computational Aeroacoustics [2,3] are capable of retaining the nonlinear character of the equations while accurately capturing the propagating waves. The CAA codes have been developed to accurately capture transient flow behavior by combining a high-accuracy spatial differencing scheme with an optimized time-marching method. Thus, they treat any unsteady problem as being a transient problem that requires high time accuracy throughout the calculation process.

On the other hand, the gust-airfoil interaction problem is an example of a periodic problem, where the exact transient solution starting from the initial conditions may not be of interest. Instead, the long-term periodic solution is usually the desired output, with the excessive accuracy of the transient calculations being redundant. In the STMA approach proposed recently by Hixon [1], an unsteady marching problem in two spatial dimensions is transformed into a steady-state iterative problem in three dimensions. At the same time, the highly convergent iterative methods from classical CFD can be applied, increasing accuracy (by using better time derivatives), reducing CPU time (because of less grid points in space-time as well as improved iterative methods), and increasing the parallel performance of the code (through larger block volumes on each processor and reduced synchronization needs during the iterative process).

* Assistant Professor, Member AIAA.

† Visiting Assistant Professor, Member AIAA.

© 2003 Golubev & Rohde. Published with permission.

A numerical study of the CAA benchmark problem of a high-intensity gust-airfoil unsteady interaction has been previously conducted in Ref. [4] using a nonlinear high-order prefactored compact CAA code implementing the low-storage 4th order 5-6 Low Dispersion and Dissipation Runge-Kutta scheme [5] for time marching, and prefactored 6th order compact scheme and explicit boundary stencils for spatial derivatives [6].

The present work revisits the problem and uses the STMA method to confirm the previous results, to obtain a more detailed picture of nonlinear interaction effects due to high-intensity gusts, and, most importantly, to examine the potential of the new computational method.

GOVERNING EQUATIONS

The unsteady, inviscid, nonlinear analysis of the high-intensity gust-airfoil interaction problem is based on the numerical solution to the unsteady Euler equations; written in Cartesian coordinates,

$$Q_t + E_x + F_y = 0,$$

$$Q = \begin{bmatrix} \rho \\ \rho u \\ \rho v \\ E \end{bmatrix}$$

$$E = \begin{bmatrix} \rho u \\ \rho u^2 + p \\ \rho uv \\ u(E + p) \end{bmatrix} \quad (1)$$

$$F = \begin{bmatrix} \rho v \\ \rho uv \\ \rho v^2 + p \\ v(E + p) \end{bmatrix}$$

where the unsteady pressure is recovered from,

$$p = (\gamma - 1) \left(E - \frac{1}{2} \rho (u^2 + v^2) \right) \quad (2)$$

In this work, the gust response is investigated for a cambered, thick Joukowski airfoil, which requires recasting the equations into generalized curvilinear coordinates. Similar to previous studies [4,7],

$$\xi = \xi(x, y)$$

$$\eta = \eta(x, y)$$

and the resulting Euler equations are of the form,

$$Q_t + \xi_x E_\xi + \eta_x E_\eta + \xi_y F_\xi + \eta_y F_\eta = 0 \quad (3)$$

The numerical study previously performed in Ref. [4] used the nonlinear high-order prefactored compact code to examine the unsteady response of both symmetric and cambered airfoils to an impinging vortical gust in the parametric space of gust dimension, intensity, and frequency. For the analysis of the nonlinear gust response problem, a C-grid 2D topology was generated for a 12% thick Joukowski airfoil. The same topology is applied in the present study.

FORMULATION FOR STMA METHOD

In the STMA process, the governing equations (1) are transformed into curvilinear coordinates that are all functions of space and time as follows:

$$\xi = \xi(x, y, t)$$

$$\eta = \eta(x, y, t) \quad (4)$$

$$\tau = \tau(x, y, t)$$

In this development, it is important to note that τ is a function of x , y , and t ; thus τ is not, in general, a time-like variable. Substituting into Eq. (1), the following equations are obtained in the strong conservation form:

$$\left(\tau_t \frac{Q}{J} + \tau_x \frac{E}{J} + \tau_y \frac{F}{J} \right)_\tau +$$

$$\left(\xi_t \frac{Q}{J} + \xi_x \frac{E}{J} + \xi_y \frac{F}{J} \right)_\xi + \quad (5)$$

$$\left(\eta_t \frac{Q}{J} + \eta_x \frac{E}{J} + \eta_y \frac{F}{J} \right)_\eta = 0$$

Note that the τ coordinate is defined in space-time in this approach, $\tau = \tau(x, y, t)$, rather than the usual definition of $\tau = \tau(t)$. Thus, there is no time-like variable in the STMA approach, and a standard time-marching approach cannot be used. Instead, an iterative method is used to solve Eq. (5). In the application to the unsteady gust-airfoil interaction problem, the periodic nature of the flow may be used to minimize the computational time and effort required to solve the test cases. For instance, the mesh is designed to cover one period of the vortical gust in the time direction, with a periodic boundary condition applied at the time inflow and time outflow boundaries. Thus, the computed solution is driven directly to the final long-term periodic solution of interest, rather than expending effort in accurately resolving the initial transient solution.

PHYSICAL MODEL FOR GUST-AIRFOIL INTERACTION AND PREVIOUS RESULTS

The unsteady, nonlinear airfoil response to an impinging vortical gust is examined for a series of imposed harmonic gust intensities and frequencies. The gust is initiated with the following distribution of perturbation velocity:

$$\begin{aligned} u_{gust} &= -\left(\frac{\varepsilon\beta M}{\sqrt{\alpha^2 + \beta^2}}\right) \cos(\alpha x + \beta y - \omega t) \\ v_{gust} &= -\left(\frac{\varepsilon\alpha M}{\sqrt{\alpha^2 + \beta^2}}\right) \cos(\alpha x + \beta y - \omega t) \end{aligned} \quad (6)$$

where ε is the gust intensity relative to the mean flow, α and β are the gust wavenumbers, and ω is the imposed gust frequency. The mean flow is defined far upstream from the airfoil as:

$$\begin{aligned} \bar{\rho} &= 1 \\ \bar{u} &= M \\ \bar{v} &= 0 \\ \bar{p} &= \frac{1}{\gamma}(\bar{\rho}^\gamma) \end{aligned} \quad (7)$$

where M is the Mach number, and $\gamma=1.4$.

The present study focuses on one particular case from a set of gust and airfoil configurations examined in Ref. [4]. In particular, a loaded, 12%-thick 2%-cambered Joukowski airfoil is considered at a two-degree angle of attack. The impinging gust is two-dimensional, with $\alpha = 2k, \beta = 2k, \omega = 2kM$ in Eq. (6).

Figure 1 illustrates the computational domain used in Ref. [4] and is applied, with a few modifications, in the current study. The shaded contour plot illustrates the instantaneous perturbation velocity contours for the 2D gust interacting with the cambered airfoil, for a reduced gust frequency $k=1$ (non-dimensionalized by the airfoil chord and the upstream flow velocity) and an intensity equal to 20% of the mean flow.

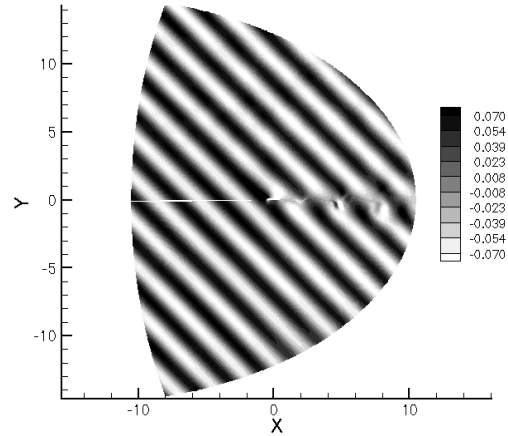


Figure 1: Instantaneous velocity, Y-component: $k=1.0$, 2D gust, $\varepsilon=0.20$, cambered airfoil (from Ref.[4]).

Results obtained in Ref. [4] for the gust reduced frequencies up to $k=1.0$ indicated a number of nonlinear effects in the unsteady airfoil response. In particular, those effects included generation of higher harmonics and combination tones associated with nonlinear self-interaction and exchange of energy between multiple imposed frequencies for gust amplitudes approaching 20% of the mean flow. Figure 2 further illustrates the predicted change in the airfoil acoustic directivity with increasing gust intensity at a distance of four chords away from the airfoil center-point. Note that, at least partially, these effects were attributed to the development of inviscid wake instability acting as a new non-compact source.

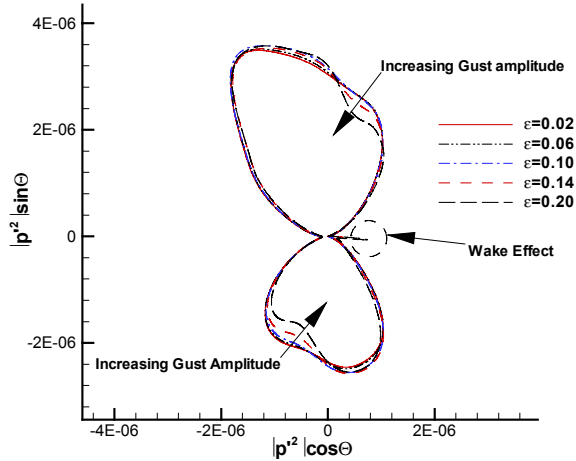


Figure 2: Effect of ϵ on $|p'|$. Distribution at $R=4$ ($k=1.0$, 2D gust, cambered airfoil (from Ref. [4]).

NUMERICAL IMPLEMENTATION

The H2 Advanced Concepts, Inc., Mapping Analysis Research Code 1 (MARC1) has been developed to solve the STMA equations [1,8]. This solver uses the Tam and Webb 7-point 4th order Dispersion Relation Preserving (DRP) scheme [2] with the 10th order artificial dissipation [3] added in all coordinate directions. To obtain the solution of Eq. (5), a time-like term may be added to the equation, and the third-order Runge-Kutta scheme of Jameson et. al. [9] can be used in combination with implicit residual smoothing and local time stepping to accelerate convergence. For the test cases presented, however, a single iterative step is used with no implicit residual smoothing. All computations were run on a mesh of $N_x * N_y * N_t = 433 * 125 * 17$. On a single-processor 2.8 GHz Linux PC station, a single case run was taking up to a week to fully converge.

RESULTS AND DISCUSSION

All results provided below are calculated for the mean flow Mach number $M=0.5$ and 2D gust reduced frequency $k=1.0$, for gust intensities ranging from $\epsilon=0.02$ to $\epsilon=0.4$. To validate the numerical computations, a comparison is conducted with the available GUST3D [10]

frequency domain linear analysis calculations. It is assumed that results for a low-intensity gust ($\epsilon=0.02$) should fall within the linear response limits, thus allowing such validation.

Figure 3 provides illustration of the computational domain along with contours of the conservative variable ρv from the solution vector Q in Eq. (1). Note that the x - y plane corresponds to the computational domain in Figure 1, with the additional time coordinate along z . The translucent contour plot thus shows the gust evolution in space and time for $\epsilon=0.2$. For the high intensity, the gust experiences notable distortions in the wake region of the airfoil.

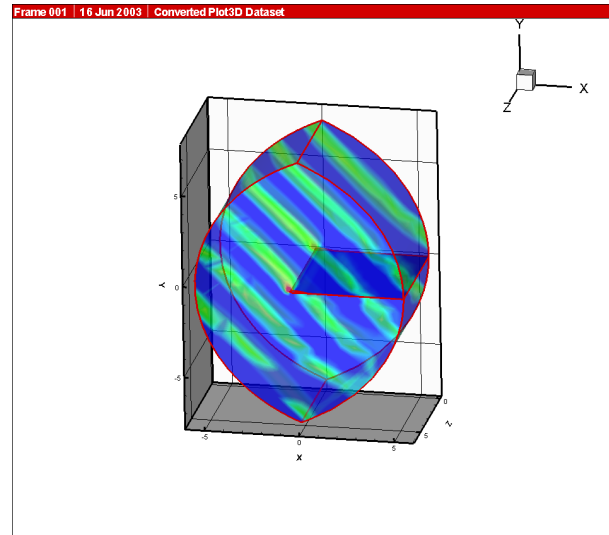


Figure 3: Instantaneous ρv -component for gust with $\epsilon=0.2$.

Aifoil Mean Pressure

Along the surface of the airfoil, the aerodynamic response contains both the mean (due to the airfoil camber and angle of attack) and unsteady perturbation (due to the incident gust) pressure components. The results for the mean pressure distribution on the suction and pressure sides are compared in Figure 4 with computations from FLO36 mean flow solver used as input in the GUST3D code. Note that the STMA results are in good agreement with the FLO36 solution, with some deviation observed near the leading edge for the highest gust intensity of $\epsilon=0.4$. In fact, the

STMA-produced pressure contours illustrated in Figures 5-6 for $\epsilon=0.02$ and 0.4 , respectively, show the presence of a shock and a small supersonic bubble in the case of the maximum gust amplitude. This produces the characteristic wiggles observed in Figure 4 near the shock region. An FFT analysis of the pressure solution did not, however, indicate any energy transfer between the mean flow and the higher frequency harmonics in this case.

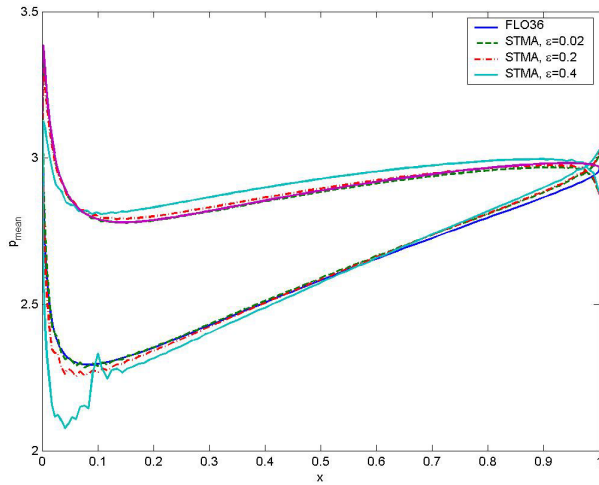


Figure 4: Airfoil mean pressure on the suction and pressure sides: comparison of FLO36 solution with STMA predictions at $\epsilon=0.02$, 0.2 and 0.4 .

Airfoil RMS Pressure

Figures 7-10 focus on the airfoil unsteady pressure RMS and FFT. A general comparison of GUST3D pressure RMS predictions with STMA computations for different gust intensities is provided in Figure 7. The response amplitudes are scaled to the same input gust amplitude to allow comparison. In all cases, the agreement is remarkable between STMA and GUST3D solutions, with small deviations observed near the trailing edge due to a local loss of numerical accuracy. It seems remarkable that moderate deviations in the mean pressure did not turn into much larger deviations in the unsteady pressure response. Moreover, the base FFT harmonic shown in Figure 8 appears to be closer to the GUST3D prediction, which is particularly

noticeable for the highest gust intensity. This may indicate a nonlinear effect. Indeed, Figures 9 and 10 provide further explanation by showing the first three FFT harmonics of the STMA solution. Note that for $\epsilon=0.4$, both higher harmonics show a significant presence in the shock region (approaching $x=0.1$), confirming the importance of nonlinear effects in this area.

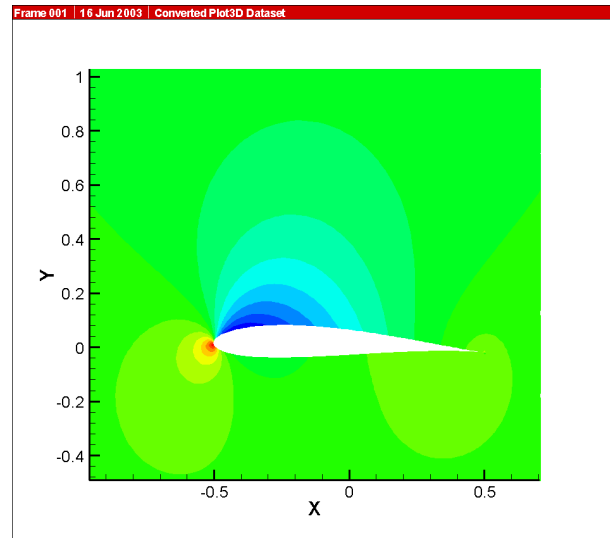


Figure 5: Mean pressure contours for $\epsilon=0.02$ (STMA calculation).

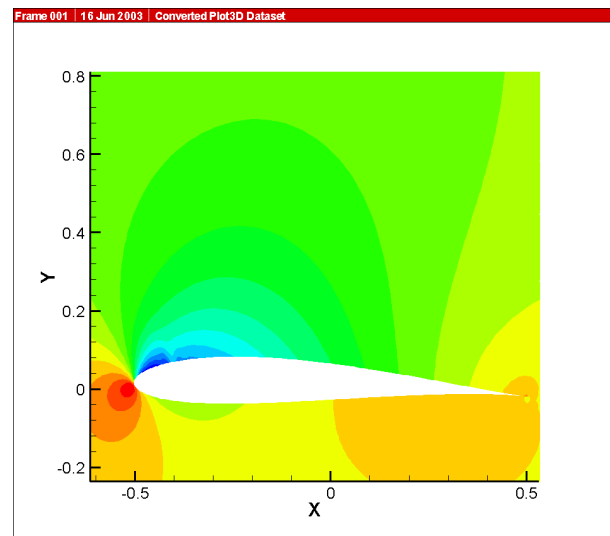


Figure 6: Mean pressure contours for $\epsilon=0.4$ (STMA calculation).

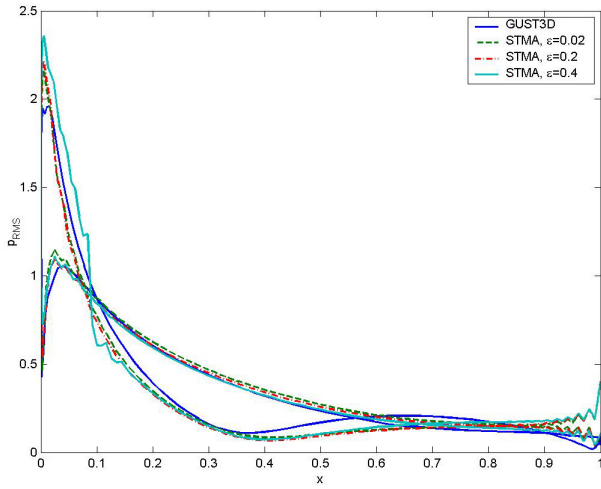


Figure 7: Airfoil RMS pressure on the suction and pressure sides: comparison of GUST3D solution with STMA predictions at $\epsilon=0.02, 0.2$ and 0.4 .

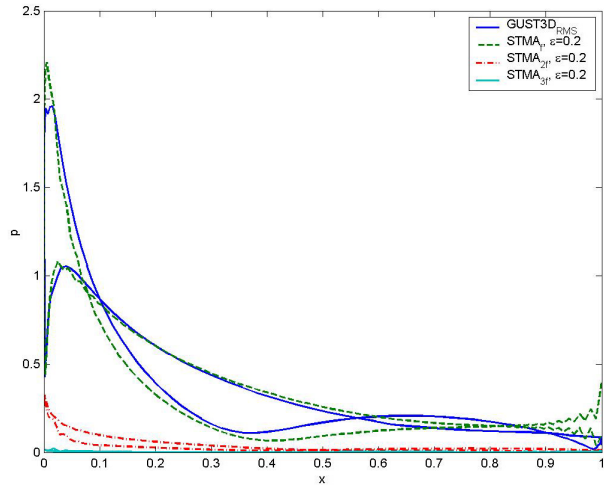


Figure 9: Base, first and second harmonics of airfoil pressure FFT on the suction and pressure sides: comparison of GUST3D RMS solution with STMA predictions at $\epsilon=0.2$.

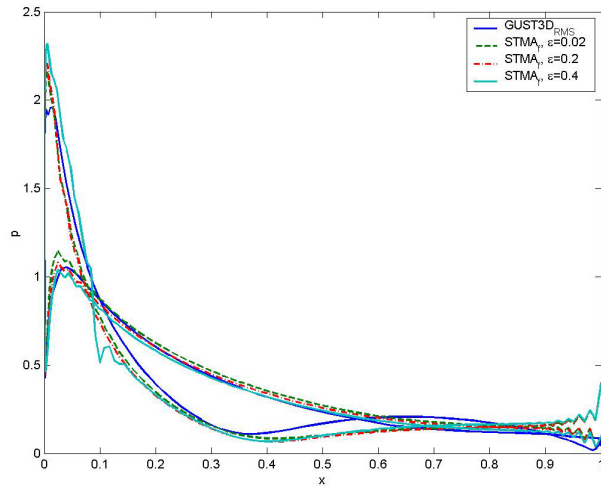


Figure 8: Base harmonic of airfoil pressure FFT on the suction and pressure sides: comparison of GUST3D RMS solution with STMA predictions at $\epsilon=0.02, 0.2$ and 0.4 .

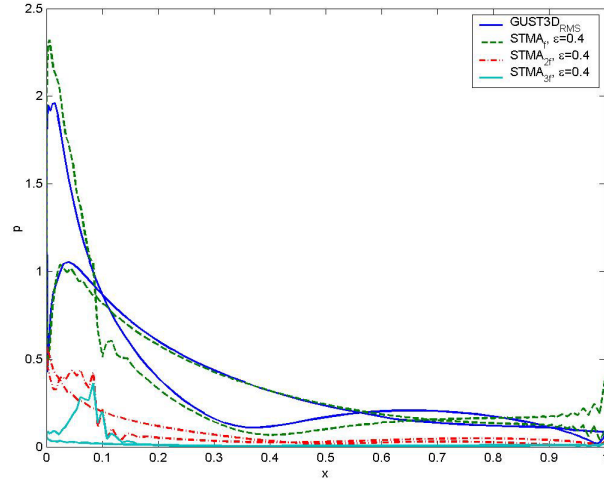


Figure 10: Base, first and second harmonics of airfoil pressure FFT on the suction and pressure sides: comparison of GUST3D RMS solution with STMA predictions at $\epsilon=0.4$.

Acoustic Directivity

The unsteady pressure predictions in the near to far fields surrounding the airfoil are illustrated in terms of the directivity contours for the predicted intensity of the unsteady pressure signal. Results shown in Figures 11-14 provide the directivity plots at radii $R=1,2,3$ and 4 , respectively (as usual, all distances are normalized by the airfoil chord, and unsteady responses are scaled by the same input gust amplitude).

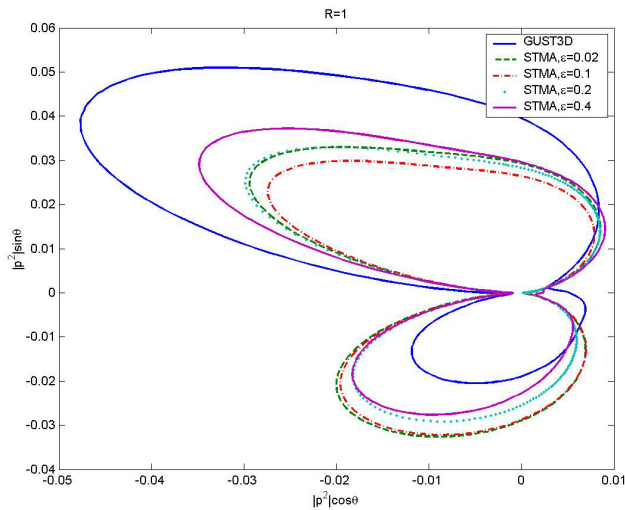


Figure 11: Directivity of $|p^2|$ for RMS pressure at $R=1$.

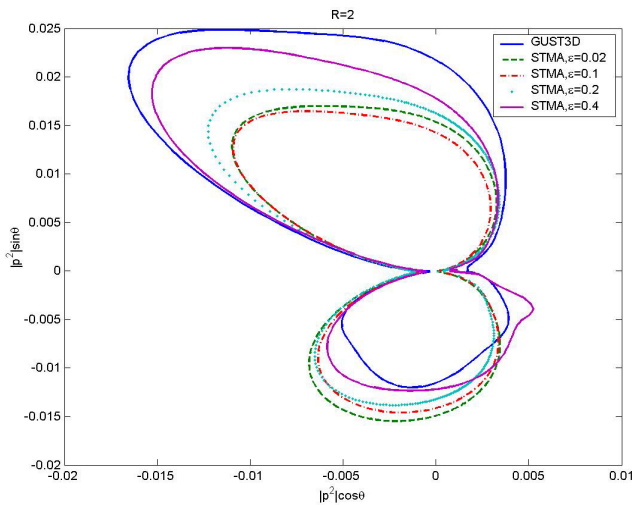


Figure 12: Directivity of $|p^2|$ for RMS pressure at $R=2$.

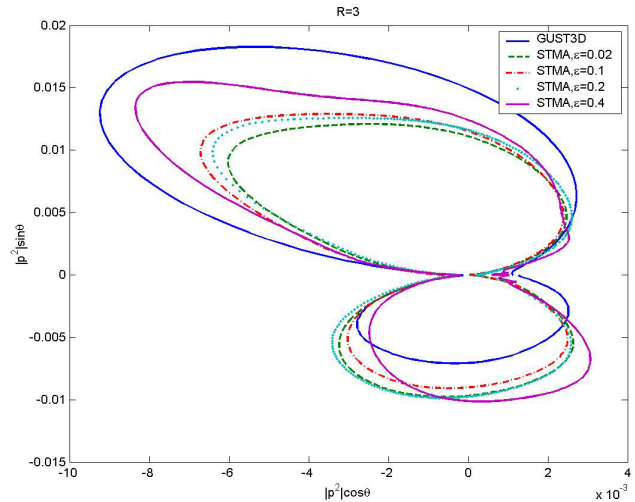


Figure 13: Directivity of $|p^2|$ for RMS pressure at $R=3$.

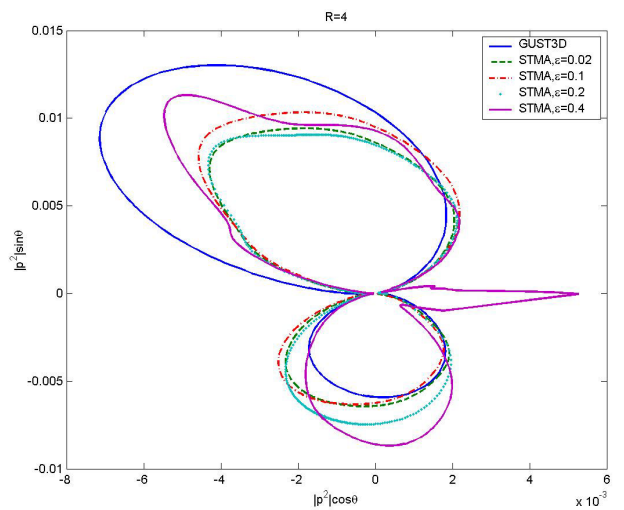


Figure 14: Directivity of $|p^2|$ for RMS pressure at $R=4$.

First, one may note significant deviations from GUST3D results observed in all cases. On the other hand, the same deviation for this gust-airfoil configuration has been observed before in Ref. [4] and was attributed to a known GUST3D problem in the far field (this problem has been recently resolved, but the relevant data has not yet been made available at the time of this publication). Most importantly, the results appear practically identical to predictions in Ref. [4]. In the current calculations, a domain of smaller size was used, and as a result, some distortions due to the

proximity of the far field boundary and inherent moderate reflections may be noticeable at $R=4$. In order to further understand the nature of these distortions (particularly noticeable for $\varepsilon=0.4$), the directivity contours were calculated for the base and first FFT harmonics of the unsteady pressure signal.

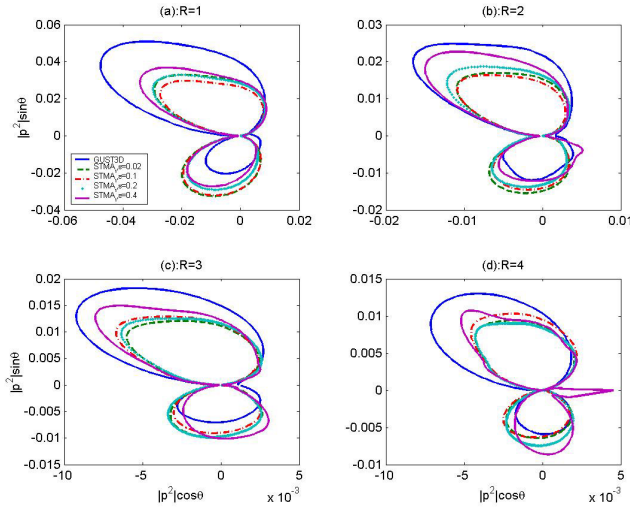


Figure 15: Directivities of $|p^2|$ for the base FFT harmonic at $R=1,2,3$ and 4 .

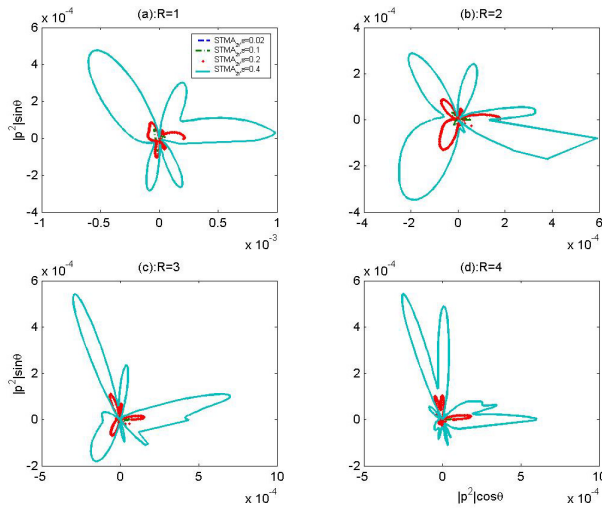


Figure 16: Directivities of $|p^2|$ for the first FFT harmonic, at $R=1,2,3$ and 4 .

Clearly, nonlinear effects increase significantly for $\varepsilon=0.4$, compared to low gust intensities (the axial spike in Figure 15d is actually due to the aerodynamic pressure from the vortex which happened to locate at $R=4$). Still, the first harmonic remains one to two orders of magnitude lower than the base harmonic. Moreover, the base shows the same distortion of the upper lobe in Figure 15d observed for the RMS pressure in Figure 14. Thus, although the higher harmonic does appear to shoot in the direction of the lobe distortion (in Figure 16d), this effect may not be completely attributed to nonlinear generation of higher harmonics. Rather, this may also indicate the appearance of a non-compact acoustic source, or problems with reflections from the far field boundary. To obtain a clearer picture of these phenomena, the contour plots of the unsteady pressure RMS and FFT are presented next.

Qualitative Analysis of Nonlinear Response

To further understand the qualitative behavior of the unsteady solution throughout the domain, the unsteady pressure contour plots are now examined. The linear response for $\varepsilon=0.02$ is observed in Figure 17. The contours show propagation of the acoustics away from the airfoil along with formation of the characteristic dipole-type radiation pattern observed in the previous directivity plots.

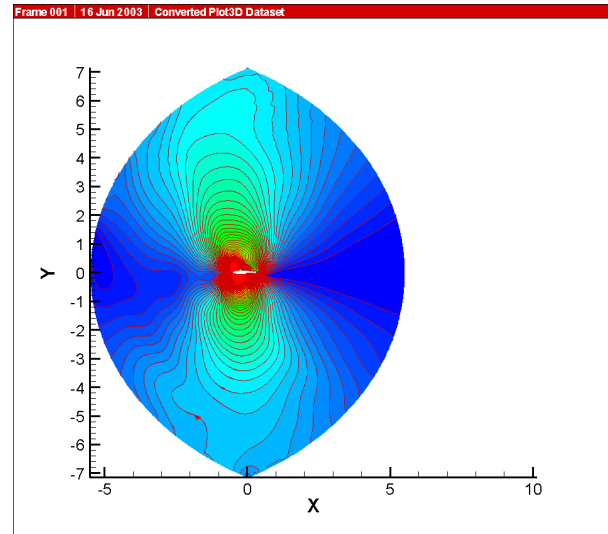


Figure 17: RMS of unsteady pressure for $\varepsilon=0.02$.

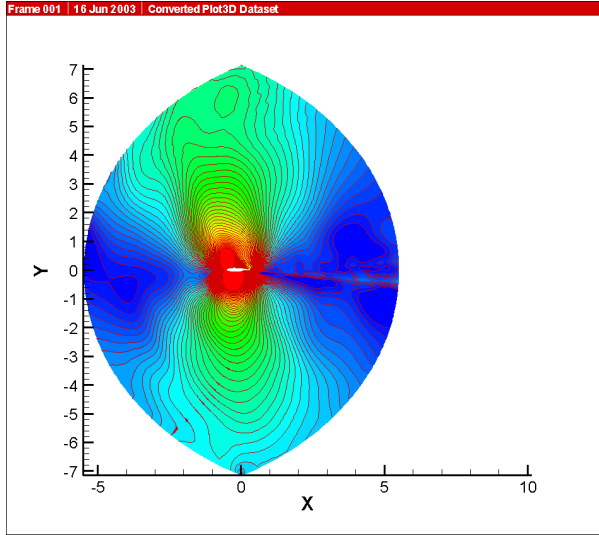


Figure 18: RMS of unsteady pressure for $\epsilon=0.2$.

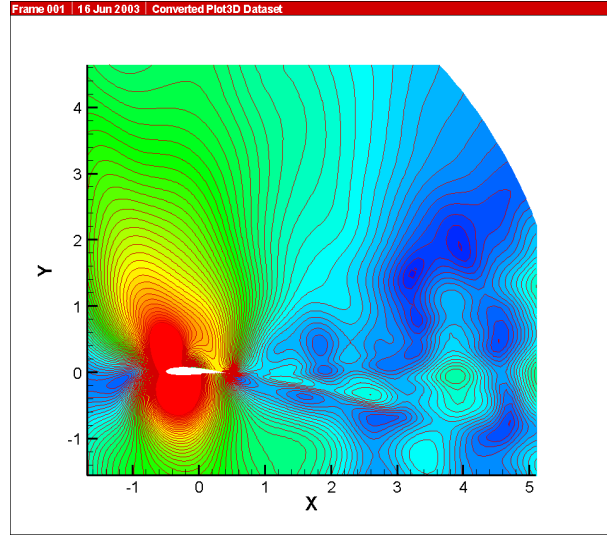


Figure 20: RMS of unsteady pressure for $\epsilon=0.4$: airfoil and wake regions.

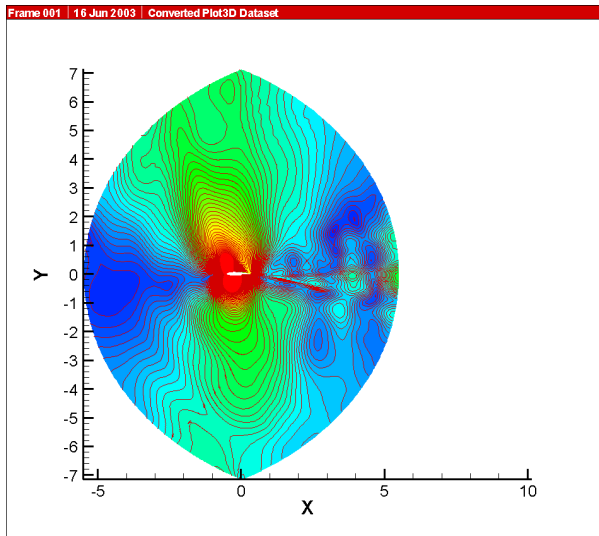


Figure 19: RMS of unsteady pressure for $\epsilon=0.4$.

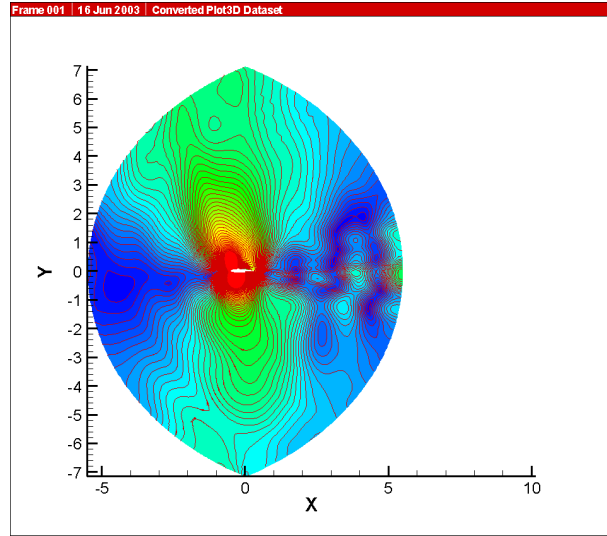


Figure 21: FFT of unsteady pressure, base harmonic, $\epsilon=0.4$.

While the previous Figure contained no (at least apparent) indication of the nonlinear wake development, both cases of $\epsilon=0.2$ and $\epsilon=0.4$ (in Figures 18 and 19) show significant effects of nonlinear wake evolution accompanied by strong aerodynamic pressure pulsations. Enlarged in Figure 20 for $\epsilon=0.4$, this region shows characteristic vortex roll-ups and pairing, indicative of a nonlinear, inviscid wake instability.

In general, acoustic radiation is known to develop from such nonlinear vortex interaction, but this is not evident from the current results. On the other hand, the presence of higher harmonics of the unsteady pressure response is confirmed by comparing the base and the first FFT harmonics of the signal in Figures 21 and 22 for $\epsilon=0.4$. The nonlinearity, exhibited by the presence of the first pressure harmonic, is clearly localized in the wake

region, but it is also seen in the direction where the directivity lobe has been observed to develop a significant distortion (in Figure 14). Hence, at least some nonlinear effect appears present in this case.

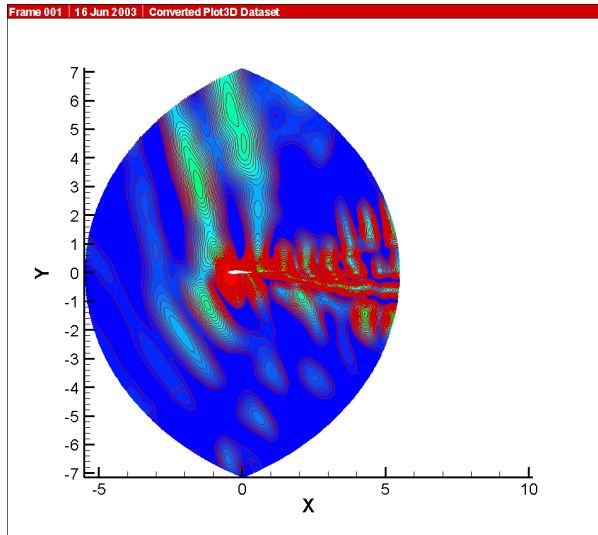


Figure 22: FFT of unsteady pressure, first harmonic, $\epsilon=0.4$.

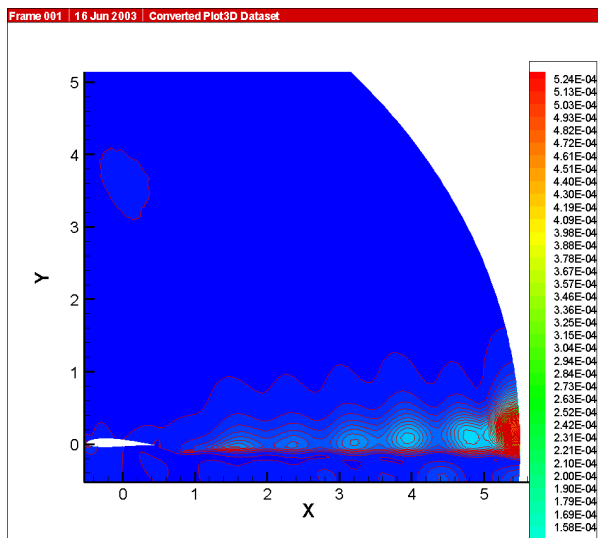


Figure 23: Difference of base frequency and linear response RMS of unsteady pressure, $\epsilon=0.02$.

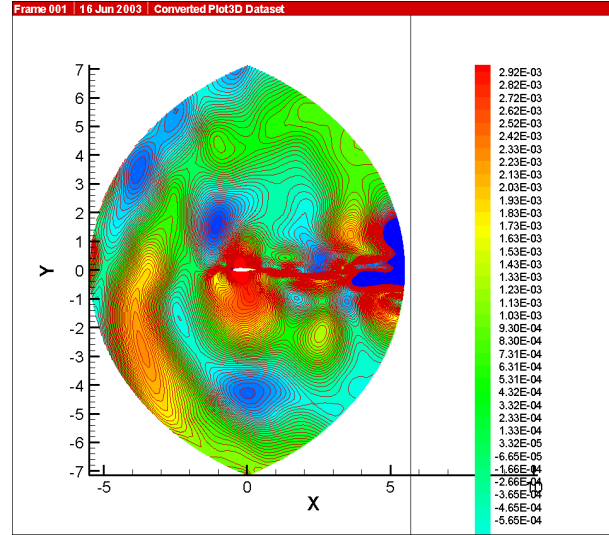


Figure 24: Difference of base frequency and linear response RMS of unsteady pressure, $\epsilon=0.2$.

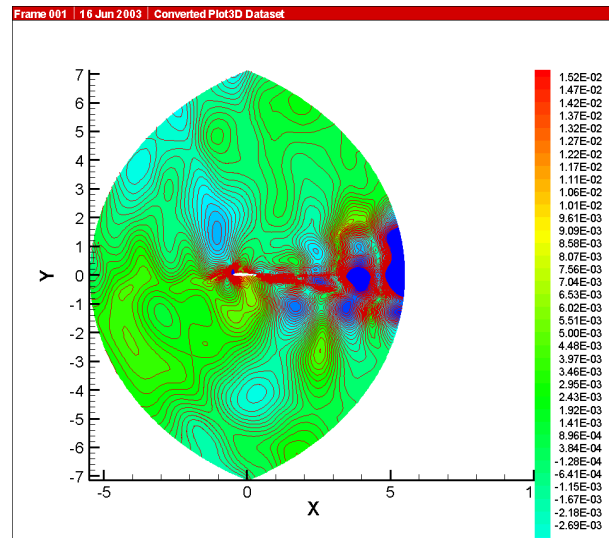


Figure 25: Difference of base frequency and linear response RMS of unsteady pressure, $\epsilon=0.4$.

Finally, in order to quantify and localize effects from nonlinear gust-airfoil interactions, the difference of the appropriately scaled (by the corresponding amplitudes, for a unit input) base frequency and RMS of unsteady linear pressure response are shown in Figures 23-25 for $\epsilon=0.02$, 0.2 and 0.4. Note that zero difference in this case is an indication of a purely linear response.

Interestingly enough, some evidence of wake nonlinearity appears present even at $\epsilon=0.02$, but the deviation from the linear behavior is very small (of the order of $1.e-4$). On the contrary, the nonlinearities are clearly present for higher gust intensities. Those are still mostly localized in the wake, but are also again seen in the region above the airfoil. The relative amplitude of these nonlinearities appears to increase from about $1.e-3$ for $\epsilon=0.2$, to approximately $1.e-2$ for $\epsilon=0.4$, which confirms the previous observations.

CONCLUSIONS

The paper examined the application of a new Space-Time Mapping Analysis (STMA) method to predict the nonlinear unsteady airfoil response to an impinging, high-intensity gust. By treating the time coordinate identically to the space directions, the STMA method essentially solved the unsteady 2D interaction problem as a steady-state 3D one. A high-order discretization scheme was applied to achieve time-accurate predictions of both unsteady aerodynamic and aeroacoustic responses.

The results for the 2D gust interaction with a cambered, thick Joukowski airfoil at an angle of attack were calculated for the mean flow Mach number $M=0.5$ and gust reduced frequency $k=1.0$, for gust intensities ranging from $\epsilon=0.02$ to $\epsilon=0.4$. To validate the numerical computations, a comparison was conducted with the frequency domain linear solver GUST3D. An excellent agreement with GUST3D data was observed for the mean and RMS pressure predictions along the airfoil surface.

Results were also obtained by localizing the zones in the computational plane where nonlinear response effects appeared most significant. Such zones have been detected primarily in the wake region, but were also observed above the airfoil. In general, for the highest gust amplitude of 40%, the nonlinear deviation did not exceed 10% of the linear values.

REFERENCES

1. Hixon, R., "Space-Time Mapping Analysis for the Accurate Calculation of Complex Unsteady Flows", AIAA Paper 2003-3205, May 2003.
2. Tam, C.K.W. and Webb, J.C., "Dispersion-Relation-Preserving Finite-Difference Schemes for Computational Acoustics", Journal of Computational Physics, Vol. 107, 1993, pp. 262-281.
3. Kennedy, C.A. and Carpenter, M.H., "Several New Numerical Methods for Compressible Shear-Layer Simulations", Applied Numerical Mathematics, Vol. 14, 1994, pp. 397-433.
4. Crivellini, A., Golubev, V.V., Mankbadi, R.R., Scott, J.R., Hixon, R. and Povinelli, L.A., "Nonlinear Analysis of Airfoil High-Intensity Gust Response Using a High-Order Prefactored Compact Code", AIAA Paper 2002-2535, Breckenridge, CO, June 2002.
5. Stanescu, D. and Habashi, W.G., "2N-Storage Low Dissipation and Dispersion Runge-Kutta Schemes for Computational Acoustics", Journal of Computational Physics, Vol. 143, 1998, pp.674-681.
6. Hixon, R., "A New Class of Compact Schemes", AIAA Paper 98-0367, Reno, NV, January 1998.
7. Hixon, R., Mankbadi, R.R. and Scott, J.R., "Validation of a High-Order Prefactored Compact Code on Nonlinear Flows with Complex Geometries", AIAA Paper 2001-1103, Reno, NV, January 2001.
8. MARC 1.11, © 2002 by H2 Advanced Concepts, Inc. Fairview Park, OH.
9. Jameson, A., Schmidt, W., and Turkel, E., "Numerical Solutions of the Euler Equations by Finite-Volume Methods Using Runge-Kutta Time-Stepping Schemes", AIAA Paper 81-1259, June 1981.
10. Scott, J.R. and Atassi, H.M., "A Finite-Difference, Frequency-Domain Numerical Scheme for the Solution of the Gust-Response Problem", Journal of Computational Physics, Vol. 119, pp.75-93, 1995.